Research Square

Preprints are preliminary reports that have not undergone peer review.
They should not be considered conclusive, used to inform clinical practice,
or referenced by the media as validated information.

Acute trifluralin exposure reveals bioenergetic and transcriptomic differences in iPSC-derived enteric neural lineages from sporadic Parkinson's disease donors

Yanlin Wang
Universitätsklinikum Erlangen
Bruno Ghirotto
Universitätsklinikum Erlangen
Vivien Ruder
Universitätsklinikum Erlangen
Anja Land
Universitätsklinikum Erlangen
Luís Eduardo Gonçalves
Universitätsklinikum Erlangen
Holger Wend
Universitätsklinikum Erlangen
Michaela Farrell
Universitätsklinikum Erlangen
Sumit Kumar
Universitätsklinikum Erlangen
Claudia Günther
Universitätsklinikum Erlangen
Markus F. Neurath
Universitätsklinikum Erlangen
Martin Regensburger
Universitätsklinikum Erlangen
Aline Bozec
Universitätsklinikum Erlangen
Beate Winner
Universitätsklinikum Erlangen
Pooja Gupta
Pooja.Gupta@uk-erlangen.de

Universitätsklinikum Erlangen

Article

Keywords: Parkinson’s disease, enteric nervous system, gut-brain axis, induced pluripotent stem cells, trifluralin, alternative splicing, mitochondrial respiration

Posted Date: November 27th, 2026

DOI: https://doi.org/10.21203/rs.3.rs-11470151/v1

License: This work is licensed under a Creative Commons Attribution 4.0 International License.
Read Full License

Additional Declarations: No competing interests reported.

Abstract

Trifluralin disrupts mitochondrial function and survival in patient-derived midbrain dopaminergic neurons. Whether this Parkinson-relevant herbicide also perturbs the enteric nervous system, a potential early site of Parkinson's disease pathology and a key component of the gut-brain axis, remains unknown. Here we tested the effect of trifluralin in induced pluripotent stem-cell-derived enteric neural lineages of four sporadic Parkinson's disease donors and three healthy controls. At baseline, RNA sequencing identified a Parkinson's disease signature characterized by immune pathway enrichment and negative enrichment of synaptic and oxidative-phosphorylation gene sets. Trifluralin elicited shared lysosomal, antigen-processing and vesicular-transport programmes, alongside donor-group-dependent inflammatory and xenobiotic-metabolism responses. Consistent with this bioenergetic signature, Parkinson's disease-derived enteric neural lineages showed lower basal and ATP-linked respiration than trifluralin-treated controls. Alternative-splicing changes were associated with intracellular trafficking, proteasomal turnover, autophagy and mitophagy, suggesting that altered RNA processing may contribute to the relationship between proteostatic stress and mitochondrial quality control. These findings extend trifluralin responsiveness beyond midbrain dopaminergic neurons and suggest that sporadic Parkinson's disease background shapes coordinated inflammatory, proteostatic and bioenergetic responses in human enteric neural cells.

Introduction

Parkinson's disease (PD) is a progressive neurodegenerative disorder characterized by bradykinesia, rigidity, and tremor together with a broad spectrum of non-motor symptoms, some of which precede motor onset [1, 2]. Most PD cases are sporadic and are thought to result from a complex interplay of ageing, genetic susceptibility, and environmental exposures [1]. Gastrointestinal dysfunction can precede the onset of motor symptoms, and α-synuclein pathology has been detected in peripheral autonomic and enteric structures. These observations have motivated body-first PD models in which pathological changes may arise outside the central nervous system in a subset of individuals, with the enteric nervous system (ENS) as a plausible early site of disease initiation [3–5].

The ENS contains interconnected neuronal and glial populations that coordinate gastrointestinal motility, secretion, barrier function, and local immune communication [4]. Its exposure to luminal and systemic signals makes it a relevant interface between environmental stress and neuronal vulnerability. Epidemiological studies have associated pesticide exposure with increased PD risk, although risks differ across compounds and exposure contexts [6, 7]. A pesticide-wide epidemiological and human induced pluripotent stem cell (iPSC) screen recently identified the dinitroaniline herbicide trifluralin as a driver of dopaminergic-neuron toxicity and mitochondrial dysfunction [8]. Whether this response extends to human enteric neural cells, and whether it is shaped by sporadic PD background, remains unknown.

Trifluralin is a synthetic, lipophilic dinitroaniline herbicide used to control annual grasses and broadleaf weeds. It disrupts plant microtubule assembly and has raised environmental concerns because of its

persistence and toxicity to non-target organisms [9, 10]. Together with evidence of mitochondrial toxicity in human dopaminergic neurons [8], this provides a mechanistic entry point for investigating the ENS. In PD, impaired bioenergetics is closely linked to defective proteostasis and lysosomal degradation, while inflammatory signalling may further modify these interconnected cellular stress responses [11, 12]. These pathways are particularly consequential in neurons, whose membrane excitability, axonal transport, synaptic transmission and protein quality control impose sustained energetic demands. Human iPSC models allow this stress network to be examined in donor-specific neural backgrounds, including sporadic disease in which no single pathogenic variant explains susceptibility [13]. Protocols deriving ENS lineages from human pluripotent stem cells generate mixed cultures containing enteric neurons and glia, providing a scalable human system in which to determine whether trifluralin triggers these disease-relevant pathways and whether the response differs between PD and control backgrounds [14, 15].

Here, we generated iPSC-derived enteric neural lineages (ENLs) from four sporadic PD donors and three neurologically healthy controls. We assessed differentiation and concentration-dependent apoptosis, then used bulk RNA sequencing, gene-set enrichment, direct group-by-treatment interaction testing, alternative-splicing analysis, RT-qPCR and mitochondrial stress testing to distinguish baseline donor-group features from trifluralin-associated responses. We asked whether PD-derived ENLs exhibit disease-associated molecular differences and whether acute trifluralin exposure reveals additional proteostatic and bioenergetic vulnerabilities, accompanied by altered inflammatory signalling.

Results

Control and sporadic PD iPSCs generate comparable enteric neural lineages with concentration-dependent responses to trifluralin

Control and sporadic PD iPSC lines were differentiated through neural crest progenitors and enteric neural crest spheroids to generate mixed ENLs (Fig. 1A). At the endpoint, cultures from both donor groups contained HuD-positive and TUBB3-positive neuronal cells together with GFAP-positive glial cells (Fig. 1A). These data confirmed generation of mixed enteric neuronal/glial cultures.

Lineage progression was evaluated by RT-qPCR at days 7, 40 and 72. *ELAVL4* and *TUBB3* expression increased from day 7 to the later differentiation stages, consistent with acquisition of neuronal features, whereas *GFAP* expression was highest at day 72, consistent with progressive glial differentiation (Fig. 1B). No donor-group difference was detected for the markers examined, supporting broadly comparable differentiation under the applied protocol.

To define the response range for downstream studies, ENLs were exposed to 90, 180 or 270 µM trifluralin for 48 h and analysed by Annexin V/propidium iodide flow cytometry (Fig. 1C). The percentage of live cells among all singlets did not differ significantly across the tested conditions. The 270 µM, 48 h

condition was subsequently used for RNA-sequencing, alternative-splicing and targeted RT-qPCR analyses, with DMSO serving as corresponding controls. This condition represents a high-concentration exposure paradigm and cannot be classified as apoptosis-associated based on the available data. Mitochondrial respiration was assessed after a shorter 6 h exposure to the same concentration.

To assess whether trifluralin treatment was associated with major shifts in inferred cellular composition, we deconvoluted the bulk RNA-sequencing data using a previously published human ENS single-cell atlas [16]. The analysis identified multiple neuronal subtypes (excitatory and inhibitory motor neurons, interneurons, sensory neurons and somatosensory neurons) and glial populations, with no marked differences in inferred proportions across conditions (Fig. 1D,E).

Figure 1. Generation and characterization of human iPSC-derived enteric neural lineages from control and sporadic PD donors and their response to trifluralin.

(A) *Schematic of the differentiation protocol used to generate enteric neural lineages (ENLs) from human induced pluripotent stem cells (iPSCs). iPSCs were differentiated through enteric neural crest (ENC) induction, ENC spheroid formation, and enteric neuronal differentiation to yield ENLs by day 70. Representative immunofluorescence images of ENLs derived from control and sporadic Parkinson's disease (PD) lines show staining for DAPI, HuD, TUBB3, and GFAP.* **(B)** *Relative mRNA expression of ELAVL4, TUBB3, and GFAP at days 7, 40, and 72 of differentiation, shown as log2Fold change relative to day 7. Expression of neuronal and glial lineage markers increased over the course of differentiation in both control and sporadic PD lines.* **(C)** *Experimental design for acute trifluralin exposure in iPSC-derived ENLs. Cultures were treated with trifluralin (TF: 90 µM, 180 µM, or 270 µM) or vehicle control (DMSO) for 48 h prior to harvesting for apoptosis analysis. Flow-cytometric quantification showed no significant differences in the percentage of live cells among singlets across the tested conditions. Control lines are shown in black and sporadic PD lines in red. Data points represent individual lines; bars indicate mean ± SEM. Statistical significance is indicated as shown in the figure. (D and E) Deconvolution of enteric neurons (D) and glia (E) populations using a previously published single cell atlas* [16] *as a reference.*

PD-associated immune and synaptic signatures are present at baseline and under trifluralin stress

Having established broadly comparable lineage differentiation, we asked whether PD-derived ENLs retained molecular differences from control ENLs. Under DMSO, differential-expression analysis identified both increased and decreased transcripts in PD-derived cultures (Fig. 2A). Among the prominent differences, PD-derived ENLs showed higher expression of *TMEM119*, *ITGBL1*, *A2M* and *NLRP2* and lower expression of *FOXG1*, *ADTRP*, *PCDHA6* and *PCDHB5*. KEGG gene-set enrichment analysis (GSEA) showed positive enrichment of inflammatory pathways, such as complement and coagulation, TNF, NOD-like receptor, NF-κB, JAK–STAT and RIG-I-like receptor signalling in PD-derived ENLs. Negative enrichment involved synaptic vesicle cycling, GABAergic, dopaminergic and cholinergic synapses, as well as oxidative phosphorylation (Fig. 2B).

The comparison between PD-derived and control ENLs under 270 μM trifluralin likewise identified numerous differentially expressed genes (Fig. 2C). Transcripts increased in PD-derived ENLs included *POM121L2*, *SNX29P1*, *TRPA1*, *LCN2*, *ADH7* and *IL6*, whereas *CYSLTR1*, *FMO1*, *KLHL40* and *CHRNG* were among the decreased transcripts. At the pathway level, there was a positive enrichment of immune-associated pathways and negative enrichment of synaptic pathways: complement and coagulation, TNF, NF-κB, RIG-I-like receptor, NOD-like receptor and JAK–STAT pathways were positively enriched, whereas synaptic vesicle cycling and GABAergic, cholinergic and dopaminergic synapse pathways were negatively enriched (Fig. 2D). The NF-κB heatmap was consistent with the positive enrichment observed in the trifluralin-treated PD-versus-control contrast, with a broader subset of pathway genes showing relatively high expression in trifluralin-treated PD-derived ENLs, particularly in donors Pat3 and Pat4 (Fig. 2E). Substantial inter-donor heterogeneity and treatment-associated expression changes in some control lines were also evident. The heatmap therefore supports enhanced NF-κB-associated expression in PD-derived ENLs under trifluralin but does not independently establish a PD-specific treatment effect; that inference requires the direct group-by-treatment contrast below.

Figure 2. Differential gene expression and pathway enrichment analysis of sporadic PD-derived ENLs under DMSO and TF treatment conditions.

(A, C) *Volcano plots showing differential gene expression between PD-derived and control ENLs under DMSO conditions (A) and following treatment with 270 μM TF (C). Upregulated transcripts in PD-derived ENLs are shown in red, downregulated transcripts in blue, and non-significant transcripts in grey. Selected differentially expressed genes are labeled. Dashed lines indicate the significance and fold-change thresholds used for differential expression analysis: adjusted P < 0.05 and |log2 fold change| >1.* **(B, D)** *KEGG gene-set enrichment analysis (GSEA) of the PD-versus-control comparison under DMSO conditions (B) and after trifluralin treatment (D). Dot size represents gene count, and color indicates adjusted P-value.* **(E)** *Heatmap of genes in the NF-κB signaling pathway across control and PD-derived ENL samples under DMSO and trifluralin-treated conditions. Rows represent individual samples and columns represent pathway genes. Sample names denote donor identity and treatment condition, with T1 corresponding to DMSO and T2 corresponding to TF. Relative expression is shown as scaled values, with red indicating higher expression and blue indicating lower expression. Annotation bars indicate donor group (control or patient) and treatment condition (DMSO or TF).*

Trifluralin is associated with shared lysosomal, ferroptotic and vesicular-transport programmes

We next examined the treatment-associated response within each donor group by comparing 270 μM trifluralin with DMSO. In control ENLs, trifluralin was associated with a broad transcriptional response that included increased expression of *ALMS1-IT1*, *HSPA6*, *DDIT3*, *CDKN1A* and *HSPA5* and decreased expression of *MIR210HG*, *LDHA*, *SULT1B1* and *LRTM1* (Fig. 3A). GSEA identified positive enrichment of

lysosome biogenesis, antigen processing and presentation, ferroptosis and SNARE interactions in vesicular transport (Fig. 3B).

PD-derived ENLs also showed a broad treatment-associated transcriptional response (Fig. 3C). *ALMS1-IT1*, *ATF3*, *DDIT3*, *ADTRP* and *FOXG1* were among the increased transcripts, whereas *FMO1*, *HSPB3*, *KLHL40* and *LRTM1* were among the decreased transcripts. As in controls, lysosome biogenesis, ferroptosis, antigen processing and presentation and SNARE interactions in vesicular transport were positively enriched; serotonergic synapse was negatively enriched in the displayed PD contrast (Fig. 3D). Expression patterns across genes assigned to lysosome biogenesis further illustrated a treatment-associated shift in both donor groups, with substantial inter-donor variability (Fig. 3E). These findings support a shared core response to the high-dose condition involving lysosomal, ferroptotic, antigen-processing and vesicular-transport programmes. Differences between the separate within-group contrasts were evaluated formally using the interaction analysis below.

Figure 3. Differential gene expression and KEGG gene set enrichment analysis of TF treatment versus DMSO in control and sporadic PD-derived ENLs.

(A, C) *Volcano plots showing differential gene expression following 270 μM TF treatment relative to DMSO in control ENLs (A) and PD-derived ENLs (C). Upregulated transcripts in TF-treated cultures are shown in red, downregulated transcripts in blue, and non-significant transcripts in grey. Selected genes are labeled. Dashed lines indicate the thresholds used to define differential expression: adjusted P < 0.05 and |log2 fold change| >1.* **(B, D)** *KEGG gene-set enrichment analysis (GSEA) of TF-versus-DMSO comparisons in control ENLs (B) and PD-derived ENLs (D). Dot size represents gene count and color indicates adjusted P-value.* **(E)** *Heatmap showing relative expression of genes within the lysosome biogenesis pathway across control and PD-derived ENL samples under DMSO and TF conditions. Relative expression is shown as scaled values, with red indicating higher expression and blue indicating lower expression. Annotation bars indicate donor group and treatment condition. Sample labels denote donor identity and treatment, with T1 corresponding to DMSO and T2 corresponding to TF.*

Donor-group-dependent transcriptional responses converge with lower respiration in trifluralin-treated PD-derived ENLs

We next examined transcriptional and functional differences between PD- and control-derived ENLs under trifluralin exposure. Analysis of the RNA-sequencing data using an interaction contrast identified genes showing donor-group-dependent responses to trifluralin (Fig. 4A). Significant interaction effects included a greater positive response for *IL6*, *IL36B*, *ADH7*, *TRPA1* and related transcripts in PD-derived ENLs and a control-direction response for *FMO1*, *MUSK*, *CYSLTR1* and *KLHL40*. These data support selected donor-group-dependent transcriptional responses, without implying that every difference observed in the separate contrasts is interaction-dependent.

RELA expression was examined by RT-qPCR as a targeted readout of NF-κB-associated signalling. *RELA* did not differ significantly between donor groups under DMSO. Under trifluralin, *RELA* expression was higher in PD-derived ENLs than in treated controls, whereas the within-group DMSO-to-trifluralin comparisons were not significant (Fig. 4B). This result supports a between-group difference under the high-dose condition but does not, on its own, establish a PD-specific treatment induction.

Oxidative-phosphorylation genes were negatively enriched in PD-derived relative to control ENLs under both DMSO and trifluralin conditions (Fig. 4C, D), and donor-level expression is shown in the corresponding heatmap (Fig. 4E). To determine whether a related functional difference was detectable during acute stress, oxygen-consumption rate was measured after 270 μM trifluralin for 6 h (Fig. 4F) using Seahorse analysis. Under DMSO, basal and ATP-linked respiration did not differ significantly between donor groups. Under trifluralin, both measures were lower in PD-derived ENLs than in treated controls (Fig. 4G). The within-group DMSO-to-trifluralin comparisons were not significant. These data therefore demonstrate lower respiratory output in trifluralin-treated PD-derived cultures relative to treated controls, rather than a statistically established trifluralin-induced decrease within PD-derived cultures.

Figure 4. TF treatment reveals altered inflammatory and mitochondrial responses in sporadic PD-derived ENLs.

(A) *Volcano plot showing genes with differential treatment responses between PD-derived and control enteric neural lineages (ENLs), based on the interaction effect (PDTF-DMSO vs ControlTF-DMSO). Genes showing greater induction in PD-derived ENLs are shown to the right, genes showing greater induction in control ENLs are shown to the left, and non-significant genes are shown in grey. Selected genes are labeled. Dashed lines indicate the thresholds used to define significance: adjusted P < 0.05 and interaction |log2 fold change| >1.* **(B)** *Relative RELA mRNA expression in sPD ENLs under DMSO and 270 μM TF conditions, shown as fold change relative to control. Bars represent group means and points represent individual samples. Statistical annotations are shown as indicated.* **(C, D)** *Gene set enrichment plots for oxidative phosphorylation in the PD-versus-control comparison under DMSO (C) and TF (D) conditions. Ranked gene distributions and enrichment scores are shown for each comparison.* **(E)** *Heatmap of genes in the oxidative phosphorylation pathway across control and PD-derived ENL samples under DMSO and TF conditions. Relative expression is shown as scaled values, with red indicating higher expression and blue indicating lower expression. Annotation bars indicate donor group and treatment condition. Sample labels denote donor identity and treatment, with T1 corresponding to DMSO and T2 corresponding to TF.* **(F)** *Oxygen consumption rate (OCR) measured in control and sporadic PD ENLs treated with DMSO or 270 μM during a mitochondrial stress assay. OCR is plotted over time following sequential injection of oligomycin, CCCP, and antimycin A/rotenone. Values are shown as pmol/min/μg protein.* **(G)** *Quantification of mitochondrial functional parameters derived from the OCR assay, including ATP production and basal respiration, in control and sporadic PD ENLs under DMSO and TF conditions. Bars represent group means and points represent individual samples. Statistical annotations are shown as indicated.*

Trifluralin-associated alternative splicing implicates intracellular trafficking and proteostasis

Because spliceosome-related expression differed across conditions, we examined transcript processing using rMATS. Expression of spliceosome-associated genes varied across donors and treatments (Fig. 5A). Across the four comparisons, skipped-exon events were the most numerous, followed by retained introns and mutually exclusive exons; alternative 3' and 5' splice-site events were less frequent (Fig. 5B). The control trifluralin-versus-DMSO comparison contained the largest number of FDR-significant events. Both the PD trifluralin-versus-DMSO and trifluralin-treated control-versus-PD comparisons also contained more events than the baseline control-versus-PD comparison. Because events were filtered by FDR without an additional absolute ΔΨ threshold, event counts are interpreted as a broad survey of the splicing landscape rather than as a count of validated, large-effect isoform switches.

GO biological process enrichment of genes with FDR-significant splicing events consistently highlighted RNA splicing, mRNA processing, and mRNA metabolic regulation across comparisons, indicating that the observed alternative splicing changes are embedded within broader post-transcriptional regulatory programs. Under trifluralin, control-versus-PD differences were additionally enriched for nucleocytoplasmic transport, intracellular protein transport, autophagy-related processes, and protein modification processes (Fig. 5C), while trifluralin-associated splicing within control ENLs showed enrichment of mRNA catabolism, post-transcriptional gene regulation, proteasomal protein catabolism, and translation-related programs (Fig. 5D). In PD-derived ENLs, enriched processes included RNA splicing, mRNA processing, translation, protein targeting, and mitotic cell-cycle-associated terms (Fig. 5E). Although classical inflammatory, mitochondrial, or PD-specific processes were not the dominant enrichment signals, the recurrent involvement of autophagy, proteostasis, intracellular trafficking, nucleocytoplasmic transport, and translation control is compatible with mechanisms that could influence inflammatory signaling, mitochondrial homeostasis, and broader neurodegeneration-relevant stress responses. Convergence across enriched biological processes does not establish causality, and individual events require prioritization by effect size, junction support and recurrence across donors before isoform-level validation.

Figure 5. Trifluralin-associated alternative splicing changes in sporadic PD-derived ENLs are enriched for RNA processing and protein homeostasis-related biological processes.

(A) *Heatmap of differentially spliced spliceosome-associated genes across control and PD-derived ENL samples under DMSO and trifluralin (TF) conditions. Relative expression is shown as scaled values, with red indicating higher expression and blue indicating lower expression. Annotation bars indicate donor group and treatment condition. Sample labels denote donor identity and treatment, with T1 corresponding to DMSO and T2 corresponding to TF.* **(B)** *Distribution of alternative splicing event types and direction of change across comparisons. Panels summarize the number of significant events detected in each comparison, stratified by event class and direction, including alternative 3′ splice site (A3SS), alternative 5′*

splice site (A5SS), mutually exclusive exons (MXE), retained introns (RI), and skipped exons (SE). Colors indicate increased inclusion, increased exclusion, or no change, as labeled. **(C–E)** *Biological process enrichment analysis of genes associated with significant alternative splicing events in the indicated comparisons. (C) PD-versus-control under TF treatment (tf_ctrl_vs_pat). (D) PD ENLs under DMSO versus TF (pat_dmso_vs_tf). (E) Control ENLs under DMSO versus TF (ctrl_dmso_vs_tf). Bar length indicates gene count and color indicates adjusted P-value.*

Discussion

This study extends previous work on trifluralin-induced toxicity in Parkinson's disease-relevant midbrain dopaminergic neurons to human iPSC-derived enteric neural lineages. We used acute trifluralin exposure as a defined environmental challenge to determine whether sporadic Parkinson's disease-derived enteric neural lineages exhibit distinct molecular and functional responses compared with control-derived cultures. Three main findings emerged. First, control and sporadic Parkinson's disease iPSCs generated broadly comparable mixed enteric neuronal and glial cultures, with no evidence of major differences in lineage-marker expression under the differentiation conditions used. Second, Parkinson's disease-derived enteric neural lineages displayed a baseline transcriptional profile characterized by positive enrichment of innate immune pathways and negative enrichment of synaptic and oxidative-phosphorylation gene sets. Third, the high-dose trifluralin condition induced shared lysosomal, ferroptotic, antigen-processing and vesicular-transport programmes in both donor groups, while interaction analysis identified selected donor-group-dependent transcriptional responses and acute mitochondrial stress testing revealed lower respiration in trifluralin-treated Parkinson's disease-derived cultures compared with treated controls. Together, these findings indicate that pre-existing differences associated with sporadic Parkinson's disease influence the cellular response to trifluralin-associated stress.

The baseline immune/synaptic signature is notable because ENS neurons and glia operate at an interface among neural, epithelial, microbial and immune compartments. Positive enrichment of NF-κB, TNF, NOD-like receptor, RIG-I-like receptor, JAK–STAT and complement-related pathways suggests that PD-derived cultures retain differences in stress- and immune-responsive programmes despite comparable lineage-marker trajectories. The corresponding negative enrichment of multiple synaptic pathways may reflect altered neuronal state, neuronal subtype composition or neuron–glia proportions that are not resolved by bulk RNA sequencing. It should not be interpreted as direct evidence of reduced synaptic function. Nonetheless, the coexistence of immune and synaptic signatures is consistent with close links between inflammatory and neuronal homeostasis in PD [12] and supports the value of mixed ENLs for studying cell-state interactions that would be absent from purified neuronal cultures.

The response to trifluralin was more convergent than the separate disease-versus-control contrasts initially suggested. Both donor groups showed enrichment of lysosome biogenesis, antigen processing and presentation, ferroptosis and SNARE-mediated vesicular transport. These programmes are compatible with a general response to chemical stress involving membrane trafficking, organelle quality

control, redox balance and protein handling. The interaction analysis then provided the appropriate statistical layer for identifying where responses diverged. *IL6* and *IL36B* showed PD-direction interaction effects, whereas *FMO1*, *MUSK* and *CYSLTR1* showed control-direction effects. These observations nominate inflammatory and xenobiotic-response pathways for follow-up, but they do not establish that *FMO1* is protective or that *IL6* mediates the respiratory phenotype. Such assignments would require perturbation or rescue experiments.

Mitochondrial function provides an important functional correlate of the transcriptomic observations. Trifluralin was previously identified as a driver of dopaminergic-neuron toxicity and mitochondrial dysfunction in a combined epidemiological and human iPSC screen [8]. Here, oxidative-phosphorylation genes were negatively enriched in PD-derived ENLs under both vehicle and trifluralin conditions, and PD-derived cultures displayed lower basal and ATP-linked respiration than controls during acute high-dose trifluralin exposure. This cross-lineage convergence is biologically interesting because mitochondrial dysfunction is recurrent in PD and has been reported in other sporadic PD iPSC models [11]. Related work in iPSC-derived ENLs also indicates that inflammatory stress can intersect with mitochondrial metabolism [18]. The present Seahorse data nevertheless show significant between-group differences under trifluralin but no significant within-group treatment effects. The defensible interpretation is therefore that PD-derived ENLs have lower respiratory performance under the tested stress condition, not that trifluralin was statistically proven to reduce respiration selectively in PD-derived cells.

The alternative-splicing analysis adds a hypothesis-generating mechanistic layer. Alternative-splicing dysregulation has been identified in PD iPSC-derived dopaminergic neurons, including events involving mitochondrial and synaptic genes [19]. trifluralin-associated splicing changes repeatedly mapped to RNA splicing, mRNA processing, and mRNA metabolic regulation, with additional enrichment in specific comparisons for nucleocytoplasmic transport, intracellular protein transport, proteasomal protein catabolism, post-translational protein modification, autophagy-related processes, translation, and protein targeting. One integrative hypothesis is that changes in RNA processing alter the abundance or localization of isoforms controlling proteostasis, intracellular trafficking, and cellular quality-control pathways, thereby influencing both inflammatory signalling and mitochondrial fitness. Mitochondrial dynamics and metabolism shape inflammatory programmes [20], PINK1–Parkin-dependent quality control links ubiquitin signalling to damaged mitochondria [21], and altered endoplasmic-reticulum proteostasis and protein trafficking can promote α-synuclein aggregation in patient-derived neurons [22]. This literature provides biological plausibility for a splicing–proteostasis–inflammation/bioenergetics bridge.

The findings should be interpreted within the resolution of the study design. Donor line was treated as the biological replicate, enabling responses to be evaluated across independent sporadic PD and control backgrounds, although the cohort size limits analysis of clinical and demographic heterogeneity. Because the ENL cultures contain neuronal and glial populations, bulk RNA sequencing captures their integrated response rather than assigning molecular changes to a specific cell type. Moreover, the 270 µM, 48 h condition represents a high-intensity trifluralin challenge; therefore, the resulting transcriptomic

and splicing profiles reflect the coordinated cellular response to substantial toxicant stress. Mitochondrial respiration was examined after 6 h to capture an earlier functional phase and is consequently complementary to, rather than temporally matched with, the 48 h molecular readouts. Future cell-type-resolved analyses and validation of prioritized splice events will further define the cellular origin and functional contribution of the pathways identified here.

Within this framework, our findings extend the investigation of trifluralin to human enteric neural lineages and reveal a response pattern shaped by sporadic PD background. Baseline immune, synaptic and oxidative-phosphorylation signatures converged with lower respiration in PD-derived ENLs under acute exposure, while trifluralin-associated transcriptional and splicing changes implicated lysosomal function, intracellular trafficking, proteasomal turnover, autophagy and mitophagy. This convergence supports a model in which altered RNA processing may contribute to the convergence of inflammatory, proteostatic and mitochondrial stress pathways in PD-derived enteric neural cells. The study therefore extends the biological effects of trifluralin beyond midbrain dopaminergic neurons and supports the use of patient-derived ENLs as a human platform for investigating how environmental stress engages disease-relevant pathways in the peripheral nervous system.

Methods

iPSC cohort and ethics

The study was approved by the local Institutional Review Board of Friedrich-Alexander-Universität Erlangen-Nürnberg (approval number 17-259-B). Seven iPSC lines were used. Four lines (UKERiC99-R1-008, UKERiAY6-R1-004, UKERi88H-R1-001 and UKERiJ2C-R1-015) were derived from donors with sporadic PD. Three lines (UKERi1JF-R1-011, UKERiO3H-R1-001 and UKERi82A-S1-004), derived from individuals without a history of neurological disease, served as age- and sex-matched controls. Donor line was treated as the biological replicate. All procedures were performed in accordance with relevant guidelines and regulations, including the Declaration of Helsinki, and informed consent for derivation and research use of the iPSC lines was obtained from all participants or their legal guardians.

hiPSC maintenance

hiPSCs were cultured on Geltrex-coated six-well plates in mTeSR Plus medium (STEMCELL Technologies) at 37°C and 5% CO_2, with medium changes every other day. Cryopreserved cells were rapidly thawed at 37°C, pelleted at 300 × *g* for 3 min and seeded in mTeSR Plus supplemented with 10 µM ROCK inhibitor (Tocris). Cells were passaged at approximately 70% confluence using ReLeSR (STEMCELL Technologies) at a ratio of 1:2 to 1:3. For cryopreservation, cells were resuspended in knockout serum replacement containing 10% DMSO and stored at − 150°C. Before ENS differentiation, hiPSCs were maintained for at least two passages in Essential 8 medium (Thermo Fisher Scientific).

Differentiation into enteric neural lineages

ENL differentiation was performed using a chemically defined protocol adapted from Barber *et al.* [15]. ENS induction began on day 0 with a nearly confluent hiPSC monolayer. Cocktail A comprised Essential 6 medium containing 10 μM SB431542, 600 nM CHIR99021, 1 ng ml^{-1} BMP4 and 1% penicillin–streptomycin; Cocktail B comprised Essential 6 containing 10 μM SB431542, 1.5 μM CHIR99021 and 1% penicillin–streptomycin; and Cocktail C comprised Cocktail B supplemented with 1 μM retinoic acid. Media were changed on days 2, 4, 6, 8 and 10 according to the stepwise induction schedule. On day 12, enteric neural crest cells were dissociated with Accutase and transferred to ultra-low-attachment plates in NC-C medium containing Neurobasal medium, N2 supplement, B27 supplement without vitamin A, GlutaMAX, MEM non-essential amino acids, 10 ng ml^{-1} FGF2, 3 μM CHIR99021 and 1% penicillin–streptomycin. On day 15, spheroids were dissociated, counted using acridine orange/propidium iodide staining with a LUNA-FL counter and seeded onto Geltrex-coated plates at 60,000 cells cm^{-2} in EN-C medium containing Neurobasal medium, N2 supplement, B27 supplement with vitamin A, GlutaMAX, MEM non-essential amino acids, 100 μM ascorbic acid, 10 ng ml^{-1} GDNF and 1% penicillin–streptomycin. Cells were differentiated for up to 90 days with medium changes twice weekly. When adherence was reduced, EN-C medium was supplemented with 0.13 mg ml^{-1} Geltrex.

Trifluralin exposure and sample collection

Exposure conditions were assay specific. For tolerability testing, day-70 ENLs were exposed to 90, 180 or 270 μM trifluralin, 0.3% DMSO or untreated medium for 48 h. RNA-sequencing, alternative-splicing and targeted RT-qPCR analyses used 270 μM trifluralin or 0.3% DMSO for 48 h. Seahorse mitochondrial-stress experiments used 270 μM trifluralin or 0.3% DMSO for 6 h. Cells harvested for RNA analysis were washed in ice-cold DPBS, collected by scraping, centrifuged at 300 × *g* for 3 min and stored at − 80°C.

RT-qPCR

Total RNA was extracted using TRIzol (Invitrogen) in combination with the RNeasy Mini Kit (Qiagen). Samples were homogenized in TRIzol, phase-separated with chloroform, and the aqueous phase was mixed with 70% ethanol before purification on RNeasy columns. For RNA-sequencing samples, on-column DNase digestion was performed using the RNase-Free DNase Set (Qiagen). RNA was eluted in RNase-free water, quantified using a NanoPhotometer NP80 (Implen) and stored at − 80°C.

cDNA was synthesized from 300 ng RNA using the QuantiTect Reverse Transcription Kit (Qiagen), including genomic DNA removal with gDNA Wipeout Buffer. Reverse transcription was performed at 42°C for 30 min, followed by enzyme inactivation at 95°C for 3 min. RT-qPCR was performed using SYBR Green chemistry on a QuantStudio 5 Real-Time PCR System (Thermo Fisher Scientific). Genes analysed included *HPRT*, *RPLP0*, *TUBB3*, *GFAP*, *ELAVL4*, *RELA*, *TNF*, *IL1B* and *IL6*. *HPRT* and *RPLP0* served as reference genes. Reactions were run in technical duplicate, and relative expression was calculated using the $2^{-}\Delta\Delta Ct$ method. Data were analysed using QuantStudio Design & Analysis Software v1.5.3 and GraphPad Prism 10. **PROVIDE PRIMER SEQUENCES IN SUPPLEMENTARY TABLE S1.**

Immunocytochemistry and image acquisition

Cells were fixed on day 72 with 4% paraformaldehyde for 30 min at room temperature, washed in DPBS, permeabilized with 0.3% Triton X-100 and blocked in 5% donkey serum. Samples were incubated overnight at 4°C with mouse anti-HuC/D (Thermo Fisher Scientific, A-21271, RRID: AB_221448; 1:200), mouse anti-TUBB3 (BioLegend, 801202, RRID: AB_2313773; 1:250) or rabbit anti-GFAP (DAKO, Z0334, RRID: AB_10013382; 1:500), followed by species-appropriate fluorophore-conjugated secondary antibodies for 2 h at room temperature. Nuclei were counterstained with DAPI, and samples were mounted in Mowiol. Imaging was performed using an Evident SR Spinning Disk microscope (Olympus) with cellSens software, and images were processed in FIJI/ImageJ. The same acquisition and display settings were applied within each marker comparison.

Apoptosis analysis by flow cytometry

Compound-associated toxicity was assessed by Annexin V/propidium iodide flow cytometry using the Annexin V-FITC Apoptosis Detection Kit (eBioscience). After 48 h of treatment, detached and adherent fractions were pooled. Cells were dissociated with Accutase, resuspended in a binding buffer and counted using a NucleoCounter NC-250. Cells were stained with Annexin V-FITC and propidium iodide, filtered and analysed on a CytoFLEX S flow cytometer (Beckman Coulter) using CytExpert v2.4.0.28. Singlets were identified by forward-scatter area versus height, and apoptotic cells were quantified from Annexin V and propidium iodide staining as shown in Fig. 1C.

RNA sequencing and preprocessing

RNA sequencing was performed on day-70 ENLs from four sporadic PD and three control donors after 48 h treatment with 270 µM trifluralin or 0.3% DMSO. Libraries were prepared using rRNA depletion and sequenced in paired-end mode (2 × 150 bp) on an Illumina NovaSeq platform (GENEWIZ Germany) to a target depth of 20 million reads per library. Raw reads were processed with fastp [23] to remove adapters, poly-N sequences and low-quality reads. Quality metrics included error rate, Q20, Q30 and GC content; all libraries had Q20 > 99% and Q30 > 96%. Clean reads were aligned to GRCh38.p12 using HISAT2 v2.2.1 [24] with the corresponding gene-annotation GTF. Gene-level counts were generated with featureCounts v2.0.6 [25]. FPKM values were generated for descriptive purposes only and were not used for differential-expression testing. Ensembl identifiers were mapped to gene symbols using biomaRt [26]. Downstream analyses were performed in R v4.3.2.

Differential expression and interaction analysis

Differential expression was performed on raw gene-level counts using DESeq2 v1.48.1 [27]. Genes with a total count of 10 or fewer across all libraries were removed. DESeq2 size-factor normalization and negative-binomial dispersion estimation were applied. Each donor contributed matched DMSO- and trifluralin-treated samples, and donor identity was included in the model to account for donor-specific transcriptional variation. Donor identity was considered the biological replicate. The model used the design formula ~ ind.n + label, where *ind.n* encoded donor identity and *label* encoded the combined donor-group/treatment condition (PD DMSO, PD TF, control DMSO, or control TF). Contrasts were extracted for PD versus control under DMSO, PD versus control under trifluralin, trifluralin versus DMSO

within controls and trifluralin versus DMSO within PD-derived ENLs. The treatment-response interaction contrast was defined as (PD trifluralin − PD DMSO) − (control trifluralin − control DMSO), testing whether the transcriptional response to trifluralin differed between PD- and control-derived ENLs.

Wald tests were used for differential-expression contrasts, and *P* values were adjusted by the Benjamini–Hochberg procedure. Genes with adjusted $P < 0.05$ and $|\log_2$ fold change$| > 1$ were classified as differentially expressed. Variance-stabilized counts generated using *vst* (blind = FALSE) were used for exploratory plots. For visualization only, limma [28] was used to adjust for inter-donor variation and depict treatment- and condition-specific expression patterns. Complete differential-expression results are provided in **SUPPLEMENTARY DATA S2**.

Gene-set enrichment analysis

KEGG GSEA was performed in R using the clusterProfiler package (version 4.16.0) using genes ranked by the DESeq2 Wald statistic for each contrast, following the GSEA framework [29] and KEGG pathway definitions [30–32]. Gene sets were filtered to a minimum size of 10 genes and a maximum size of 500 genes. KEGG analysis was run using gseKEGG() with Benjamini–Hochberg adjustment to identify enriched gene sets. Positive and negative normalized enrichment scores indicate enrichment toward opposite ends of the ranked gene list and are not interpreted as direct measurements of pathway activation or inhibition. Heatmaps show row-scaled, variance-stabilized expression for genes in selected enriched pathways. For the figures, pathways were selected to summarize the recurrent immune, synaptic, lysosomal, ferroptotic, trafficking and mitochondrial themes described in the text; the complete enrichment output, including normalized enrichment scores, adjusted *P* values and leading-edge genes, are provided as **SUPPLEMENTARY DATA S3**.

Alternative-splicing analysis

Alternative splicing was analysed using rMATS-turbo v4.3.0 [33] on aligned paired-end BAM files and the GRCh38.p12 gene-annotation GTF. Replicate-aware comparisons included trifluralin versus DMSO within control and PD-derived ENLs and control versus PD-derived ENLs within each treatment condition. Skipped exons, mutually exclusive exons, retained introns, alternative 5' splice sites and alternative 3' splice sites were evaluated. Inclusion-level differences (ΔΨ) were calculated from rMATS JCEC output, which incorporates junction and exon-body counts. Events with FDR < 0.05 were retained; no additional absolute ΔΨ threshold was applied. Genes carrying significant events were tested for downstream Gene Ontology Biological Process (GO-BP) enrichment in R using clusterProfiler v4.16.0 with enrichGO(ont = "BP"), after mapping gene symbols to Entrez Gene IDs with org.Hs.eg.db v3.21.0. The background gene universe was defined as the union of all genes with tested alternative splicing events across all comparisons in the study. Multiple testing was controlled using the Benjamini–Hochberg procedure. Complete event-level results, including ΔΨ, junction counts and FDR, and the complete GO-BP enrichment output should be provided as **SUPPLEMENTARY DATA S4.**

iPSC-ENL Deconvolution for Enteric Neuronal and Glial Signatures

To estimate the relative proportions of enteric neuronal and glial populations in bulk RNA-sequencing samples, MuSiC (v1.0.0) deconvolution was performed using a previously published human ENS single-cell reference atlas [16]. Two reference datasets were used, comprising 14 annotated neuronal populations and 5 glial populations. The neuronal reference included PEMN_1–4, PIMN_1–5, PIN_1–2, PSVN_1–2, and PSN, while the glial reference included Glia_1–5. Cell-type-specific expression profiles were generated from the single-cell references using $\mu sic_b asis$, with subject identity incorporated to account for inter-subject variation.

To reduce collinearity among closely related populations, hierarchical clustering was performed separately for neuronal and glial populations using Euclidean distance and complete linkage. Neuronal populations were grouped into five macro-clusters: C1 (PEMN_1–4), C2 (PIMN_1–5), C3 (PIN_1–2), C4 (PSVN_1–2), and C5 (PSN). Glial populations were grouped into four macro-clusters: C1 (Glia_5), C2 (Glia_4), C3 (Glia_3), and C4 (Glia_1–2). Marker genes from the corresponding cell populations were combined within each macro-cluster. Bulk and single-cell reference gene identifiers were harmonized by conversion of Ensembl identifiers to HGNC gene symbols, followed by clustered deconvolution using the MuSiC music_prop.cluste function.

Seahorse mitochondrial stress test

Mitochondrial respiration was assessed using the Seahorse XF Cell Mito Stress Test Kit on a Seahorse XFe24 Analyzer (Agilent). Sensor cartridges were hydrated overnight in Seahorse XF Calibrant at 37°C in a CO_2-free incubator. ENLs were analysed on day 70–71 after 6 h exposure to 270 µM trifluralin or 0.3% DMSO. Before measurement, cells were incubated for 1 h in Seahorse XF DMEM assay medium supplemented with 1 mM pyruvate, 2 mM glutamine and 10 mM glucose. Oligomycin, CCCP and a rotenone/antimycin A mixture were sequentially injected at 5 µM each. After measurement, cells were lysed in RIPA buffer, and oxygen-consumption rates were normalized to protein concentration determined by BCA assay. Basal respiration, maximal respiration, proton leak, ATP-linked respiration, spare respiratory capacity and non-mitochondrial respiration were calculated using standard Seahorse equations.

Statistical analysis of non-omics data

Analyses were performed using GraphPad Prism 10, with donor line treated as the biological replicate. Comparisons involving more than two conditions were analysed by one-way ANOVA. Grouped datasets were analysed by two-way ANOVA followed by Sidak's or Tukey's multiple-comparison test, as appropriate. Tests were two-sided, and α was 0.05. Data are presented as mean ± SEM in the current figures. Because the donor-level sample sizes were small, individual donor values are displayed.

Use of generative artificial intelligence

A large language model was used for language editing, structural revision and journal-formatting support. The authors reviewed and verified the manuscript content, references, analyses and interpretations and take full responsibility for the submitted work.

Data availability

The RNA-sequencing data generated in this study will be available in the European Genome-phenome Archive under accession (EGAD50000003276). The dataset can be accessed by reviewers during the peer-review process via the following reviewer-specific link: https://ega-archive.org/reviewers/7edbc54b7ceb8031e7753e02163ef3e8/datasets/EGAD50000003276. Source data supporting the non-omics figures and complete differential-expression, enrichment and alternative-splicing analysis results should accompany the submission as Supplementary Data S1–S4. Additional materials are available from the corresponding author subject to the consent and material-transfer restrictions applicable to the human iPSC lines.

Code availability

No new software or algorithms were developed. Custom R and analysis scripts used to generate the reported results will be archived at https://github.com/guptalab-erlangen/parkinsons_trifluralin.git .

Declarations

Acknowledgements

Funded by the Deutsche Forschungsgemeinschaft (DFG, German Research Foundation) – 505539112 – KFO 5024 (A01, A02, A04, B02, Z01). Y.W. was supported by SFB/TRR369 “DIONE” (Project-ID 501752319, Project Z02) and the BMFTR ACS iIMMUNE project (01EO2105). S.K was supported by the AI-PREDICT project (grant no. 01ZU2502) funded by the BMFTR. A.B. was supported by SFB 1755 “CASCAID” (Project-ID 550296805, Project 01) and SFB/TRR369 “DIONE” (Project-ID 501752319, Project B05). P.G. was supported by the AI-PREDICT project (grant no. 01ZU2502) funded by the BMFTR, as well as by Deutsche Forschungsgemeinschaft (DFG, German Research Foundation) through TRR 417 (Project-ID 540805631, Project S03) and SFB 1755 “CASCAID” (Project-ID 550296805, Project Z01).

Funding

This work was supported by the Deutsche Forschungsgemeinschaft (DFG, German Research Foundation) (grant numbers 505539112 [KFO 5024; Projects A01, A02, A04, B02 and Z01], 540805631 [TRR 417; Project S03], and 550296805 [SFB 1755 “CASCAID”; Projects 01 and Z01]); the BMFTR (ACS iIMMUNE, grant number 01EO2105; AI-PREDICT, grant number 01ZU2502); and SFB/TRR369 “DIONE” (grant number 501752319; Projects Z02 and B05).

Author contributions

Y.W. analyzed and interpreted the data, executed the bioinformatics analyses, created the figures, and wrote the manuscript. B.G. performed experiments, analyzed and interpreted the data, and contributed to writing the manuscript. V.R. performed experiments and analyzed the data. A.L., L.E.G. contributed to the experimental work and data collection. H.W. and M.F. maintained iPSC cultures. S.K. contributed to the

analysis. C.G., M.N., M.R., A.B., and B.W. provided resources and supervised the project. P.G. wrote the manuscript, analyzed and interpreted the data, and supervised the bioinformatics analyses. All authors critically reviewed and approved the final version of the manuscript.

Competing interests

The authors declare no competing interests.

References

1. Poewe, W. et al. Parkinson disease. *Nat. Rev. Dis. Primers*. **3**, 17013. https://doi.org/10.1038/nrdp.2017.13 (2017).
2. Armstrong, M. J. & Okun, M. S. Diagnosis and treatment of Parkinson disease. *JAMA* **323**, 548–560. https://doi.org/10.1001/jama.2019.22360 (2020).
3. Horsager, J. & Borghammer, P. Brain-first vs. body-first Parkinson's disease: an update on recent evidence. *Parkinsonism Relat. Disord*. **122**, 106101. https://doi.org/10.1016/j.parkreldis.2024.106101 (2024).
4. Sharkey, K. A. & Mawe, G. M. The enteric nervous system. *Physiol. Rev.* **103**, 1487–1564. https://doi.org/10.1152/physrev.00018.2022 (2023).
5. Braak, H. et al. Staging of brain pathology related to sporadic Parkinson's disease. *Neurobiol. Aging*. **24**, 197–211. https://doi.org/10.1016/S0197-4580(02)00065-9 (2003).
6. Tanner, C. M. et al. Rotenone, paraquat, and Parkinson's disease. *Environ. Health Perspect.* **119**, 866–872. https://doi.org/10.1289/ehp.1002839 (2011).
7. Ascherio, A. et al. Pesticide exposure and risk for Parkinson's disease. *Ann. Neurol.* **60**, 197–203. https://doi.org/10.1002/ana.20904 (2006).
8. Paul, K. C. et al. A pesticide and iPSC dopaminergic neuron screen identifies and classifies Parkinson-relevant pesticides. *Nat. Commun.* **14**, 2803. https://doi.org/10.1038/s41467-023-38215-z (2023).
9. Giglio, A. & Vommaro, M. L. Dinitroaniline herbicides: a comprehensive review of toxicity and side effects on animal non-target organisms. *Environ. Sci. Pollut Res. Int.* **29**, 76687–76711. https://doi.org/10.1007/s11356-022-23169-4 (2022).
10. Grover, R., Wolt, J. D., Cessna, A. J. & Schiefer, H. B. Environmental fate of trifluralin. *Rev. Environ. Contam. Toxicol.* **153**, 1–64. https://doi.org/10.1007/978-1-4612-2302-3_1 (1997).
11. Cabral-Costa, J. V. & Kowaltowski, A. J. Neurological disorders and mitochondria. *Mol. Aspects Med.* **71**, 100826. https://doi.org/10.1016/j.mam.2019.10.003 (2020).
12. Tansey, M. G. et al. Inflammation and immune dysfunction in Parkinson disease. *Nat. Rev. Immunol.* **22**, 657–673. https://doi.org/10.1038/s41577-022-00684-6 (2022).
13. Takahashi, K. et al. Induction of pluripotent stem cells from adult human fibroblasts by defined factors. *Cell* **131**, 861–872. https://doi.org/10.1016/j.cell.2007.11.019 (2007).

14. Fattahi, F. et al. Deriving human ENS lineages for cell therapy and drug discovery in Hirschsprung disease. *Nature* **531**, 105–109. https://doi.org/10.1038/nature16951 (2016).
15. Barber, K., Studer, L. & Fattahi, F. Derivation of enteric neuron lineages from human pluripotent stem cells. *Nat. Protoc.* **14**, 1261–1279. https://doi.org/10.1038/s41596-019-0141-y (2019).
16. Drokhlyansky, E. et al. The Human and Mouse Enteric Nervous System at Single-Cell Resolution. *Cell* **182**, 1606–1622. https://doi.org/10.1016/j.cell.2020.08.003 (2020). e23.
17. Schmidt, S. et al. A reversible state of hypometabolism in a human cellular model of sporadic Parkinson's disease. *Nat. Commun.* **14**, 7674. https://doi.org/10.1038/s41467-023-42862-7 (2023).
18. Ghirotto, B. et al. TNF alpha unmasks enteric malate aspartate shuttle dysfunction bridging Parkinson disease and intestinal inflammation. *Nat. Commun.* **17**, 3217. https://doi.org/10.1038/s41467-026-71317-y (2026).
19. Lin, L. et al. Molecular features underlying neurodegeneration identified through in vitro modeling of genetically diverse Parkinson's disease patients. *Cell. Rep.* **15**, 2411–2426. https://doi.org/10.1016/j.celrep.2016.05.022 (2016).
20. Rambold, A. S. & Pearce, E. L. Mitochondrial dynamics at the interface of immune cell metabolism and function. *Trends Immunol.* **39**, 6–18. https://doi.org/10.1016/j.it.2017.08.006 (2018).
21. Pickrell, A. M. & Youle, R. J. The roles of PINK1, parkin, and mitochondrial fidelity in Parkinson's disease. *Neuron* **85**, 257–273. https://doi.org/10.1016/j.neuron.2014.12.007 (2015).
22. Stojkovska, I. et al. Rescue of α-synuclein aggregation in Parkinson's patient neurons by synergistic enhancement of ER proteostasis and protein trafficking. *Neuron* **110**, 436–451. https://doi.org/10.1016/j.neuron.2021.10.032 (2022). .e11.
23. Chen, S., Zhou, Y., Chen, Y. & Gu, J. fastp: an ultra-fast all-in-one FASTQ preprocessor. *Bioinformatics* **34**, i884–i890. https://doi.org/10.1093/bioinformatics/bty560 (2018).
24. Kim, D., Paggi, J. M., Park, C., Bennett, C. & Salzberg, S. L. Graph-based genome alignment and genotyping with HISAT2 and HISAT-genotype. *Nat. Biotechnol.* **37**, 907–915. https://doi.org/10.1038/s41587-019-0201-4 (2019).
25. Liao, Y., Smyth, G. K. & Shi, W. featureCounts: an efficient general purpose program for assigning sequence reads to genomic features. *Bioinformatics* **30**, 923–930. https://doi.org/10.1093/bioinformatics/btt656 (2014).
26. Durinck, S., Spellman, P. T., Birney, E. & Huber, W. Mapping identifiers for the integration of genomic datasets with the R/Bioconductor package biomaRt. *Nat. Protoc.* **4**, 1184–1191. https://doi.org/10.1038/nprot.2009.97 (2009).
27. Love, M. I., Huber, W. & Anders, S. Moderated estimation of fold change and dispersion for RNA-seq data with DESeq2. *Genome Biol.* **15**, 550. https://doi.org/10.1186/s13059-014-0550-8 (2014).
28. Ritchie, M. E. et al. limma powers differential expression analyses for RNA-sequencing and microarray studies. *Nucleic Acids Res.* **43**, e47. https://doi.org/10.1093/nar/gkv007 (2015).

29. Subramanian, A. et al. Gene set enrichment analysis: a knowledge-based approach for interpreting genome-wide expression profiles. *Proc. Natl Acad. Sci. USA*102, 15545–15550; (2005). https://doi.org/10.1073/pnas.0506580102
30. Kanehisa, M., Furumichi, M., Sato, Y., Kawashima, M. & Ishiguro-Watanabe, M. KEGG for taxonomy-based analysis of pathways and genomes. *Nucleic Acids Res.* **51**, D587–D592. https://doi.org/10.1093/nar/gkac963 (2023).
31. Kanehisa, M., Sato, Y., Kawashima, M., Furumichi, M. & Tanabe, M. KEGG as a reference resource for gene and protein annotation. *Nucleic Acids Res.* **44**, D457–D462. https://doi.org/10.1093/nar/gkv1070 (2016).
32. Kanehisa, M. & Goto, S. K. E. G. G. Kyoto Encyclopedia of Genes and Genomes. *Nucleic Acids Res.* **28**, 27–30. https://doi.org/10.1093/nar/28.1.27 (2000).
33. Shen, S. et al. rMATS: robust and flexible detection of differential alternative splicing from replicate RNA-Seq data. *Proc. Natl Acad. Sci. USA*111, E5593–E5601; (2014). https://doi.org/10.1073/pnas.1419161111

Figures

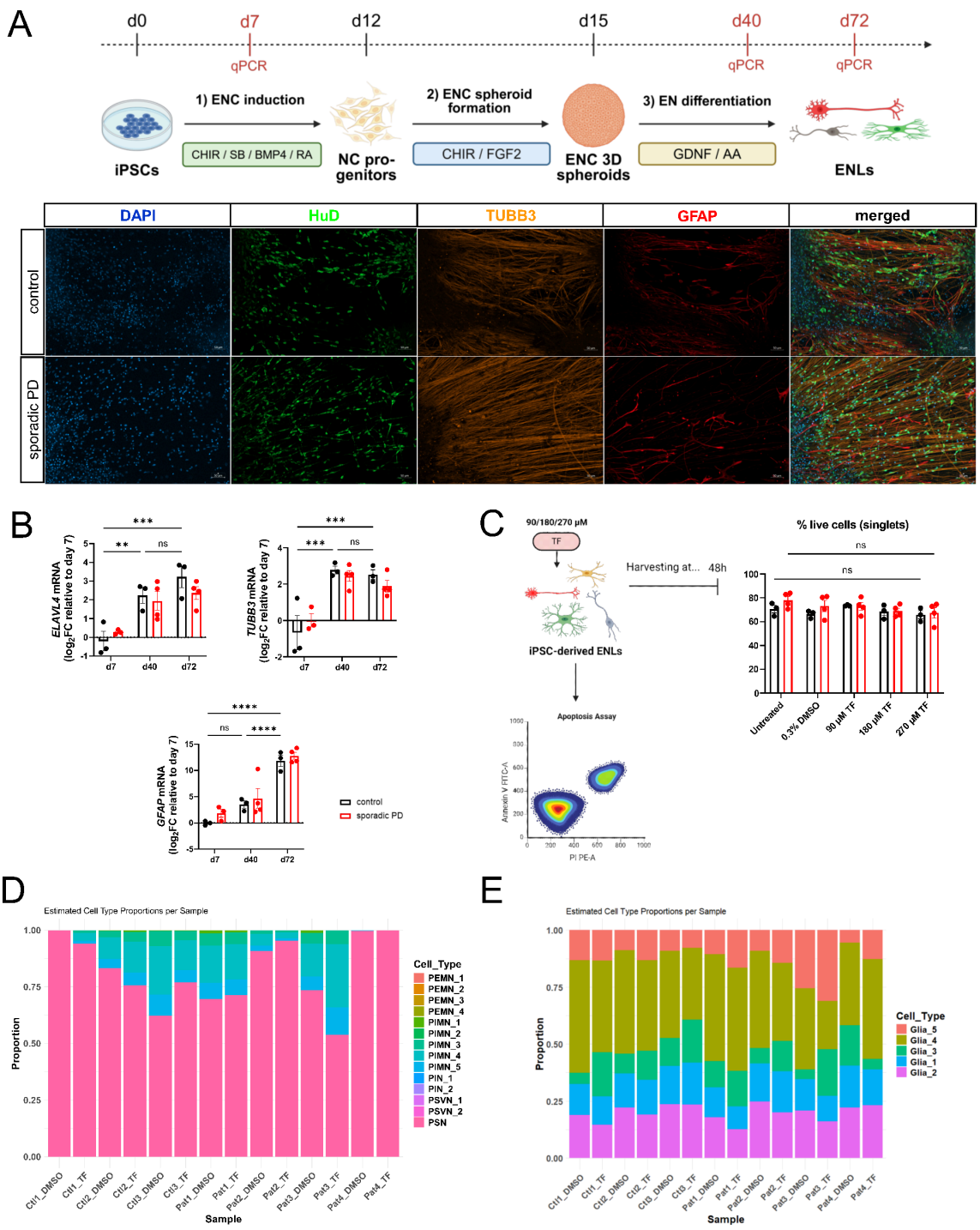

Figure 1

Generation and characterization of human iPSC-derived enteric neural lineages from control and sporadic PD donors and their response to trifluralin.

(A) *Schematic of the differentiation protocol used to generate enteric neural lineages (ENLs) from human induced pluripotent stem cells (iPSCs). iPSCs were differentiated through enteric neural crest (ENC)*

induction, ENC spheroid formation, and enteric neuronal differentiation to yield ENLs by day 70. Representative immunofluorescence images of ENLs derived from control and sporadic Parkinson's disease (PD) lines show staining for DAPI, HuD, TUBB3, and GFAP. ***(B)*** *Relative mRNA expression of ELAVL4, TUBB3, and GFAP at days 7, 40, and 72 of differentiation, shown as log2Fold change relative to day 7. Expression of neuronal and glial lineage markers increased over the course of differentiation in both control and sporadic PD lines.* ***(C)*** *Experimental design for acute trifluralin exposure in iPSC-derived ENLs. Cultures were treated with trifluralin (TF: 90 μM, 180 μM, or 270 μM) or vehicle control (DMSO) for 48 h prior to harvesting for apoptosis analysis. Flow-cytometric quantification showed no significant differences in the percentage of live cells among singlets across the tested conditions. Control lines are shown in black and sporadic PD lines in red. Data points represent individual lines; bars indicate mean ± SEM. Statistical significance is indicated as shown in the figure. (D and E) Deconvolution of enteric neurons (D) and glia (E) populations using a previously published single cell atlas [16] as a reference.*

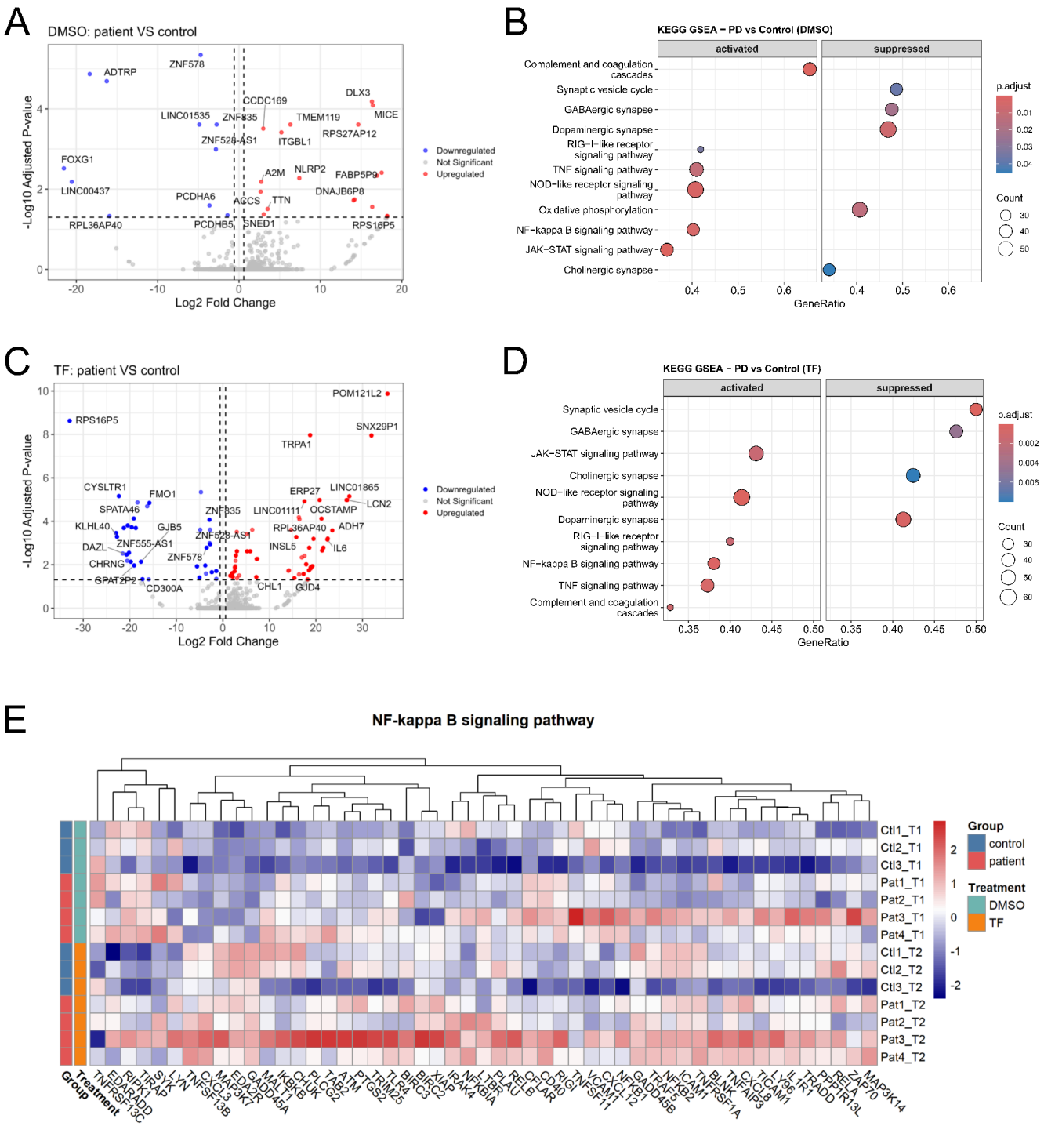

Figure 2

Differential gene expression and pathway enrichment analysis of sporadic PD-derived ENLs under DMSO and TF treatment conditions.

(A, C) *Volcano plots showing differential gene expression between PD-derived and control ENLs under DMSO conditions (A) and following treatment with 270 μM TF (C). Upregulated transcripts in PD-derived*

ENLs are shown in red, downregulated transcripts in blue, and non-significant transcripts in grey. Selected differentially expressed genes are labeled. Dashed lines indicate the significance and fold-change thresholds used for differential expression analysis: adjusted P<0.05 and |log2 fold change| >1. ***(B, D)*** *KEGG gene-set enrichment analysis (GSEA) of the PD-versus-control comparison under DMSO conditions (B) and after trifluralin treatment (D). Dot size represents gene count, and color indicates adjusted P-value.* ***(E)*** *Heatmap of genes in the NF-κB signaling pathway across control and PD-derived ENL samples under DMSO and trifluralin-treated conditions. Rows represent individual samples and columns represent pathway genes. Sample names denote donor identity and treatment condition, with T1 corresponding to DMSO and T2 corresponding to TF. Relative expression is shown as scaled values, with red indicating higher expression and blue indicating lower expression. Annotation bars indicate donor group (control or patient) and treatment condition (DMSO or TF).*

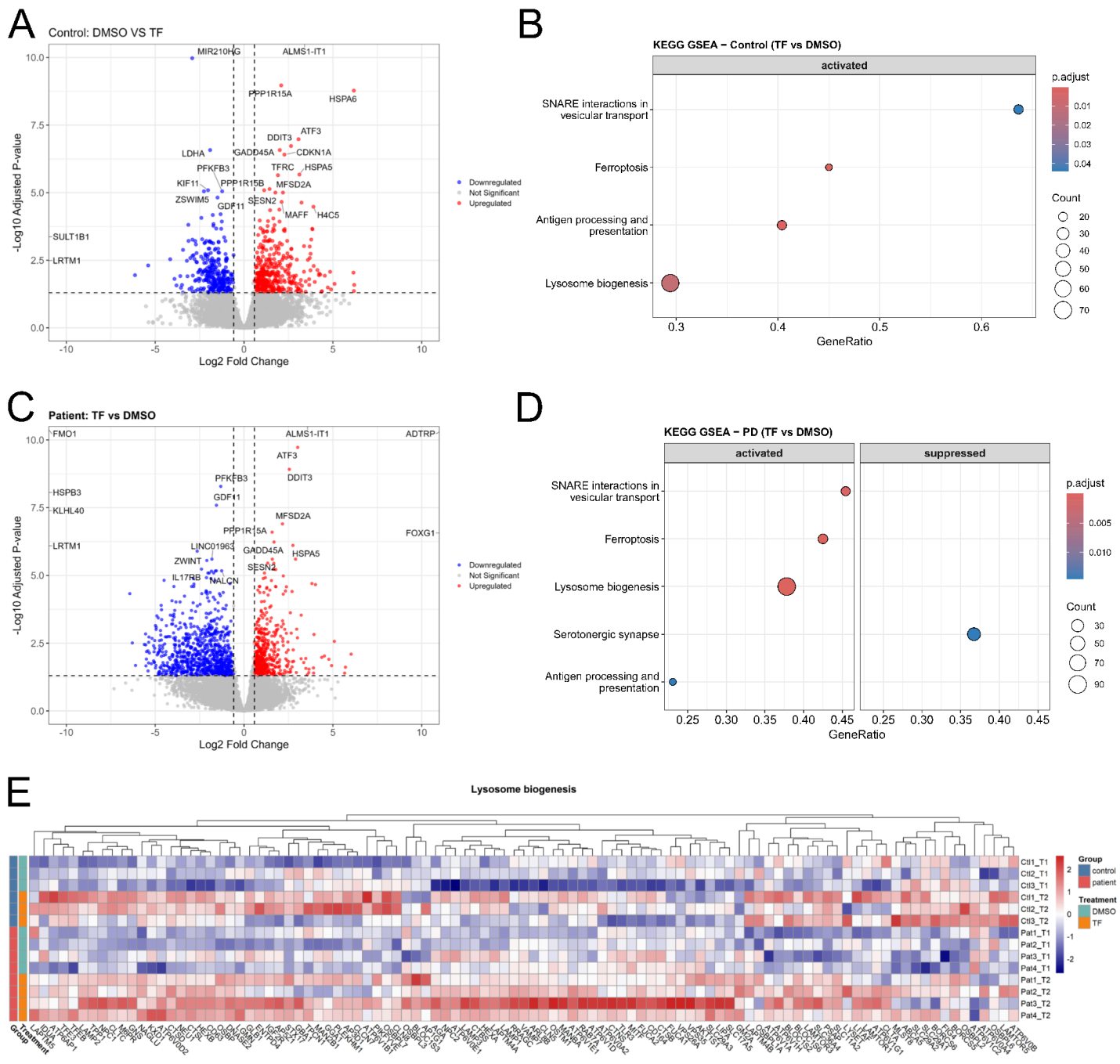

Figure 3

Differential gene expression and KEGG gene set enrichment analysis of TF treatment versus DMSO in control and sporadic PD-derived ENLs.

(A, C) *Volcano plots showing differential gene expression following 270 μM TF treatment relative to DMSO in control ENLs (A) and PD-derived ENLs (C). Upregulated transcripts in TF-treated cultures are shown in red, downregulated transcripts in blue, and non-significant transcripts in grey. Selected genes are labeled. Dashed lines indicate the thresholds used to define differential expression: adjusted P<0.05 and |log2 fold change| >1.* ***(B, D)*** *KEGG gene-set enrichment analysis (GSEA) of TF-versus-DMSO comparisons in control*

ENLs (B) and PD-derived ENLs (D). Dot size represents gene count and color indicates adjusted P-value. ***(E)*** *Heatmap showing relative expression of genes within the lysosome biogenesis pathway across control and PD-derived ENL samples under DMSO and TF conditions. Relative expression is shown as scaled values, with red indicating higher expression and blue indicating lower expression. Annotation bars indicate donor group and treatment condition. Sample labels denote donor identity and treatment, with T1 corresponding to DMSO and T2 corresponding to TF.*

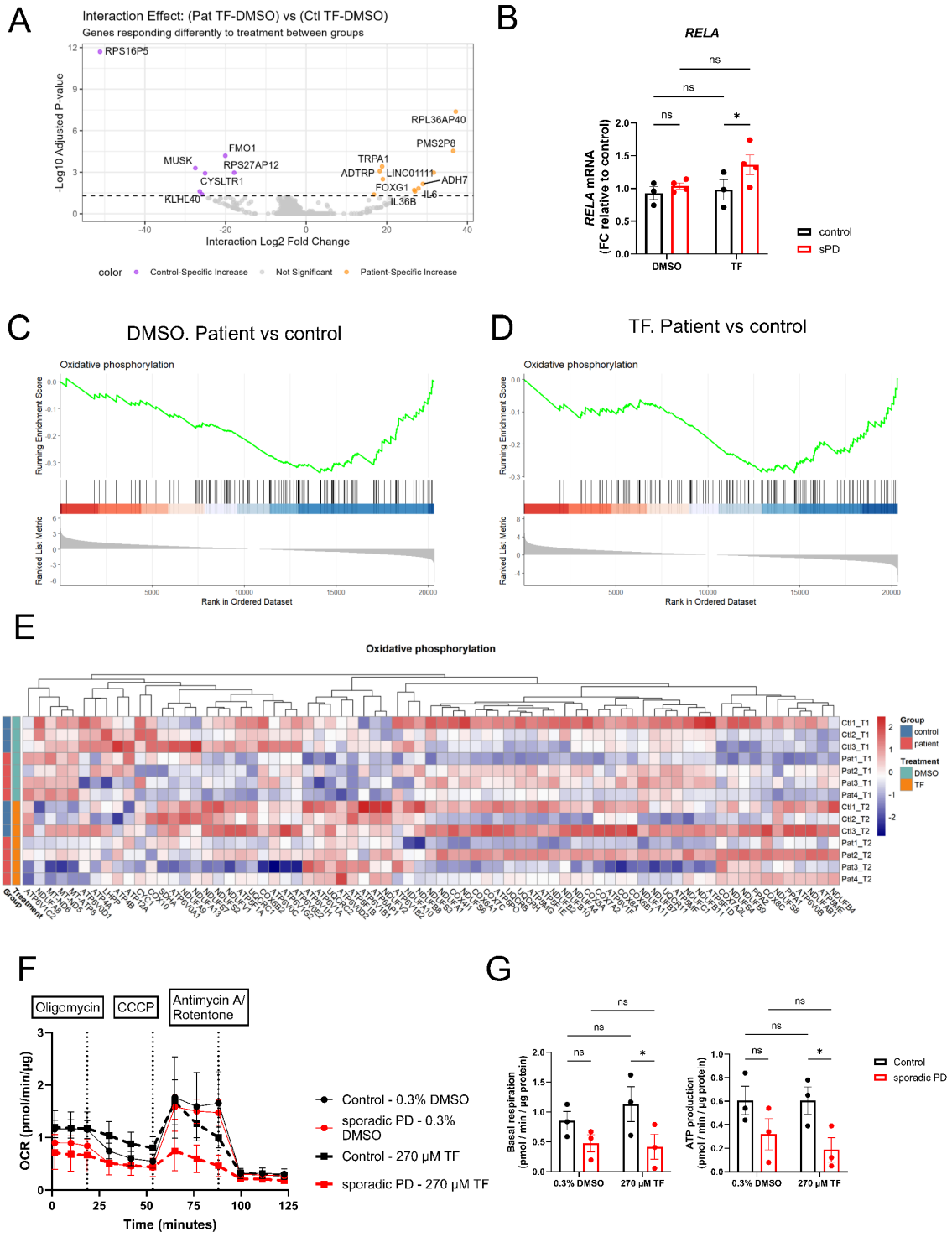

Figure 4

TF treatment reveals altered inflammatory and mitochondrial responses in sporadic PD-derived ENLs.

(A) *Volcano plot showing genes with differential treatment responses between PD-derived and control enteric neural lineages (ENLs), based on the interaction effect (PDTF-DMSO vs ControlTF-DMSO). Genes showing greater induction in PD-derived ENLs are shown to the right, genes showing greater induction in control ENLs are shown to the left, and non-significant genes are shown in grey. Selected genes are labeled. Dashed lines indicate the thresholds used to define significance: adjusted P<0.05 and interaction |log2 fold change| >1.* ***(B)*** *Relative RELA mRNA expression in sPD ENLs under DMSO and 270 μM TF conditions, shown as fold change relative to control. Bars represent group means and points represent individual samples. Statistical annotations are shown as indicated.* ***(C, D)****Gene set enrichment plots for oxidative phosphorylation in the PD-versus-control comparison under DMSO (C) and TF (D) conditions. Ranked gene distributions and enrichment scores are shown for each comparison.* ***(E)*** *Heatmap of genes in the oxidative phosphorylation pathway across control and PD-derived ENL samples under DMSO and TF conditions. Relative expression is shown as scaled values, with red indicating higher expression and blue indicating lower expression. Annotation bars indicate donor group and treatment condition. Sample labels denote donor identity and treatment, with T1 corresponding to DMSO and T2 corresponding to TF.* ***(F)*** *Oxygen consumption rate (OCR) measured in control and sporadic PD ENLs treated with DMSO or 270 μM during a mitochondrial stress assay. OCR is plotted over time following sequential injection of oligomycin, CCCP, and antimycin A/rotenone. Values are shown as pmol/min/μg protein.* ***(G)*** *Quantification of mitochondrial functional parameters derived from the OCR assay, including ATP production and basal respiration, in control and sporadic PD ENLs under DMSO and TF conditions. Bars represent group means and points represent individual samples. Statistical annotations are shown as indicated.*

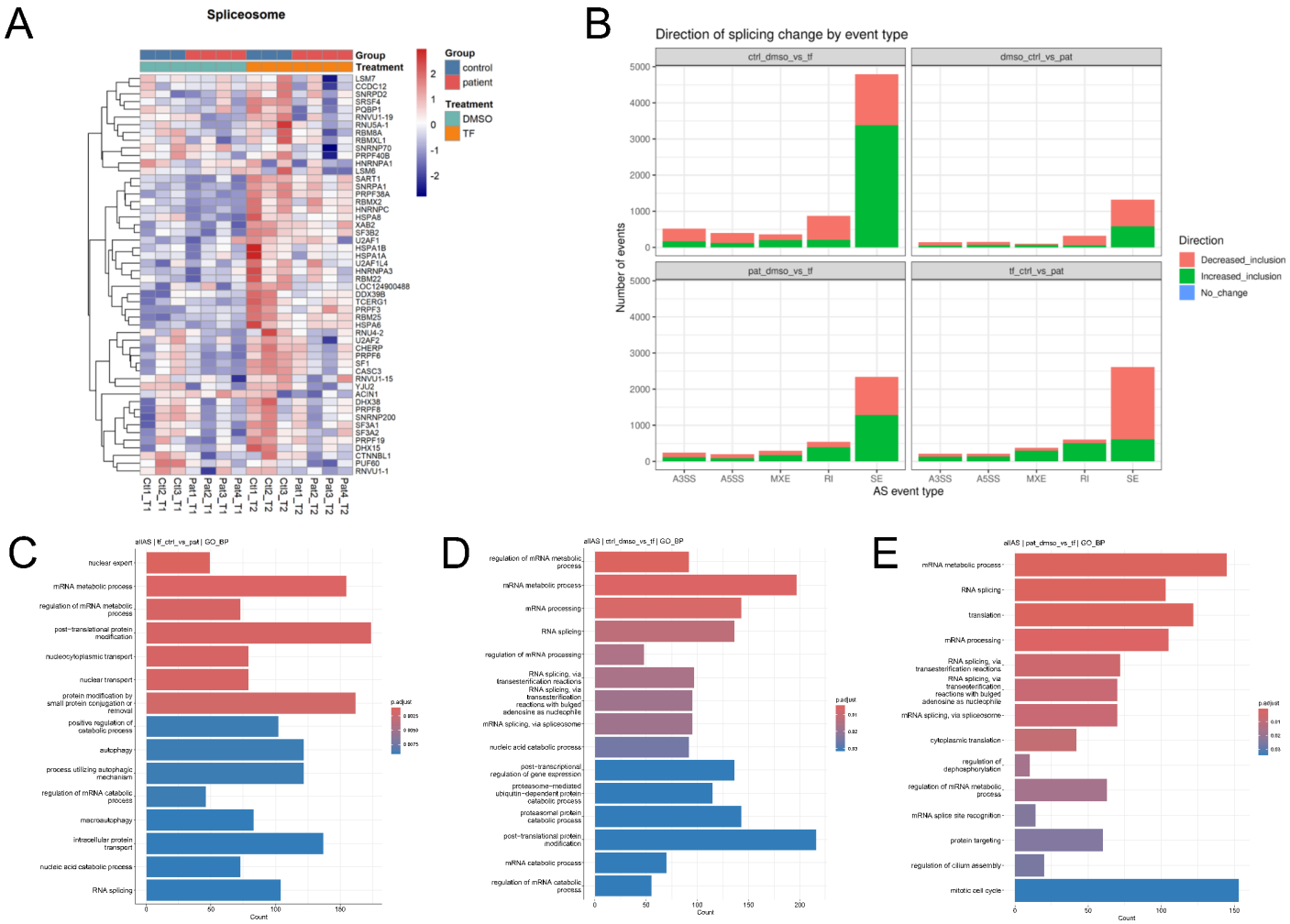

Figure 5

Trifluralin-associated alternative splicing changes in sporadic PD-derived ENLs are enriched for RNA processing and protein homeostasis-related biological processes.

(A) *Heatmap of differentially spliced spliceosome-associated genes across control and PD-derived ENL samples under DMSO and trifluralin (TF) conditions. Relative expression is shown as scaled values, with red indicating higher expression and blue indicating lower expression. Annotation bars indicate donor group and treatment condition. Sample labels denote donor identity and treatment, with T1 corresponding to DMSO and T2 corresponding to TF.* ***(B)*** *Distribution of alternative splicing event types and direction of change across comparisons. Panels summarize the number of significant events detected in each comparison, stratified by event class and direction, including alternative 3' splice site (A3SS), alternative 5' splice site (A5SS), mutually exclusive exons (MXE), retained introns (RI), and skipped exons (SE). Colors indicate increased inclusion, increased exclusion, or no change, as labeled.* ***(C–E)****Biological process enrichment analysis of genes associated with significant alternative splicing events in the indicated comparisons. (C) PD-versus-control under TF treatment (tf_ctrl_vs_pat). (D) PD ENLs under DMSO versus TF (pat_dmso_vs_tf). (E) Control ENLs under DMSO versus TF (ctrl_dmso_vs_tf). Bar length indicates gene count and color indicates adjusted P-value.*

Supplementary Files

This is a list of supplementary files associated with this preprint. Click to download.

- Supplementaryinformation.docx
- SUPPLEMENTARYDATAS1.xlsx
- SUPPLEMENTARYDATAS4.xlsx
- SUPPLEMENTARYDATAS3.xlsx
- SUPPLEMENTARYDATAS2.xlsx